Bumps and rings in a two-dimensional neural field: splitting and rotational instabilities

M. R. Owen†, C. R. Laing‡ and S. Coombes†

E-mail: markus.owen@nottingham.ac.uk

E-mail: c.r.laing@massey.ac.nz

E-mail: stephen.coombes@nottingham.ac.uk
† School of Mathematical Sciences, University of Nottingham, Nottingham, NG7 2RD, UK
‡ Institute of Information and Mathematical Sciences, Massey University, Private Bag 102-904, North Shore Mail Centre, Auckland, New Zealand

Abstract.
   In this paper we consider instabilities of localised solutions in planar neural field firing rate models of Wilson-Cowan or Amari type. Importantly we show that angular perturbations can destabilise spatially localised solutions. For a scalar model with Heaviside firing rate function we calculate symmetric one-bump and ring solutions explicitly and use an Evans function approach to predict the point of instability and the shapes of the dominant growing modes. Our predictions are shown to be in excellent agreement with direct numerical simulations. Moreover, beyond the instability our simulations demonstrate the emergence of multi-bump and labyrinthine patterns.

   With the addition of spike-frequency adaptation, numerical simulations of the resulting vector model show that it is possible for structures without rotational symmetry, and in particular multi-bumps, to undergo an instability to a rotating wave. We use a general argument, valid for smooth firing rate functions, to establish the conditions necessary to generate such a rotational instability. Numerical continuation of the rotating wave is used to quantify the emergent angular velocity as a bifurcation parameter is varied. Wave stability is found via the numerical evaluation of an associated eigenvalue problem.

1. Introduction

The mammalian cortex is often regarded as a two dimensional sheet of densely interconnected neurons, with interactions between neurons mediated by chemical synapses. Much of the activity in developing and studying continuum models of such synaptically interacting networks can be traced back to the seminal work of Wilson and Cowan [35, 36] and Amari [1, 2]. The non-local nature of neuronal interactions (arising from long-range axonal connections) means that the natural framework for developing such models has relied upon integral or integro-differential equations. Moreover, by neglecting any spatial heterogeneity, such non-local interactions have often been described using the notion of a spatial convolution of the macroscopic state variable with a kernel chosen to mimic known anatomy. This macroscopic state variable is typically interpreted as a mean firing rate, which is itself some sigmoidal function of synaptic activity. For a recent review of the dynamics of neural field models, particularly in one dimension see [6]. Of particular interest have been single population models with local excitation and distal inhibition, mimicking the behaviour of interacting excitatory and inhibitory neural sub-populations. This so-called Mexican hat connectivity is now known to underly the generation of both spatially periodic [10, 30, 4] and spatially localised structures [18, 21]. Interestingly spatially localized bumps of persistent activity have been linked to working memory (the temporary storage of information within the brain) [5, 14, 32]. In many models of working memory, transient stimuli are encoded by feature-selective persistent neural activity. Such stimuli are imagined to induce the formation of a spatially localized bump of persistent activity (which coexists with a stable uniform state).

In comparison to the studies of one dimensional networks, far less is known about behaviour of spatially localised solutions in two dimensions. Relatively recently, however, Laing and Troy [20] have developed PDE methods to study neural field equations in two spatial dimensions. This has shed a great deal of light on the conditions for the existence and stability of rotationally symmetric solutions, and in particular bump and ring structures. The challenge is open to develop alternative techniques that can address identical issues for models in the more general integral equation framework. In this paper we take a step in this direction. For a specific choice of Heaviside firing rate function, with threshold h, we construct explicit examples of previously classified ring and bump solutions [31, 34]. Moreover, we show how to treat stability to angular perturbations using a powerful Evans function approach [8]. Importantly this flags up how an extra spatial dimension can lead to fundamentally new solution instabilities. In particular we show that bump solutions may split into multiple spots under variation of the threshold parameter h. Moreover, single and multiple rings are typically found to be unstable. By direct numerical simulations of the full nonlinear integral model we show that our Evans function approach correctly predicts the number of resulting spots found beyond an instability. In the presence of linear adaptation such non-rotationally symmetric states have previously been observed to undergo bifurcations to rotating

waves‡. We show that the underlying mechanism for this bifurcation can be traced to a second real eigenvalue of the linearisation crossing through zero (the first one persisting because of an underlying rotational symmetry of the full model). In fact we use this degeneracy of eigenvalues to define the bifurcation condition for a rotational instability. Assuming the existence of a non-rotationally symmetric solution we show that, for an arbitrary firing rate function, all such solutions undergo a rotational instability at the same point in parameter space (irrespective of their detailed shape). Once again the predictions of our analysis are shown to be in excellent agreement with the results of direct numerical simulations. Moreover, numerical continuation of the rotating wave is used to quantify the emergent angular velocity as a bifurcation parameter is varied. Wave stability is found via the numerical evaluation of an associated eigenvalue problem.

In section 2 we introduce the two-dimensional scalar neural field model that we will study throughout this paper. We focus on the construction of rotationally symmetric (bump and ring) solutions in section 3, and show how explicit solutions can be easily constructed when the firing rate function is chosen to be a Heaviside. Furthermore, this restriction allows us to make precise statements about solution stability using an Evans function approach. This same machinery for predicting the onset of an instability is also used to predict the type of state that will emerge beyond bifurcation (by considering the shape of the most unstable eigenmode). In section 4 we quantify the change in state as the system evolves from one unstable localised solution to another stable one by computing an appropriate Lyapunov functional. Next, in section 5 we consider a commonly adopted description of neural adaptation, resulting in a vector model, and show that this may cause a non-rotationally symmetric solution to go unstable in favour of a stable rotating wave. Finally, in section 6 we discuss natural extensions of the work presented in this paper.

2. Two dimensional neural field model

We consider a neural field model with synaptic activity $u = u(\mathbf{r}, t)$, $\mathbf{r} = (r, \theta)$ ($r \in \mathbb{R}^+$, $\theta \in [0, 2\pi)$, $t \in \mathbb{R}^+$), governed by the integral equation

$$u = \eta * w \otimes f(u). \tag{1}$$

Here, the symbol $*$ represents a temporal convolution in the sense that

$$(\eta * f)(\mathbf{r}, t) = \int_0^t \mathrm{d}s\, \eta(s) f(\mathbf{r}, t - s), \tag{2}$$

and $\otimes$ represents a two-dimensional spatial convolution such that

$$(w \otimes f)(\mathbf{r}, t) = \int_{\mathbb{R}^2} \mathrm{d}\mathbf{r}' w(\mathbf{r} - \mathbf{r}') f(\mathbf{r}', t). \tag{3}$$

The function $\eta(t)$ (with $\eta(t) = 0$ for $t < 0$) represents a synaptic filter, whilst $w(\mathbf{r})$ is a synaptic footprint describing the anatomy of network connections. The function

‡ This was first observed numerically in unpublished work of Laing and Troy, and an original example may be found at http://www.math.pitt.edu/~troy/

f represents the firing rate of a single neuron. The focus of our study will be on the existence and stability of time-independent solutions, which satisfy

$$q(\mathbf{r}) = \int_{\mathbb{R}^2} d\mathbf{r}' w(\mathbf{r} - \mathbf{r}') f(q(\mathbf{r}')). \tag{4}$$

Assuming that one can solve this nonlinear convolution equation for a spatially localised solution, one is led naturally to the question of stability. To ascertain this we linearise about the time-independent solution by writing $u(\mathbf{r}, t) = q(\mathbf{r}) + u(\mathbf{r})e^{\lambda t}$ and expand to first order in $u(\mathbf{r})$ to obtain

$$u(\mathbf{r}) = \text{LT}[\eta](\lambda) \int_{\mathbb{R}^2} d\mathbf{r}' w(\mathbf{r} - \mathbf{r}') f'(q(\mathbf{r}')) u(\mathbf{r}'), \tag{5}$$

where $\text{LT}[\eta](\lambda)$ is the Laplace transform of $\eta(t)$:

$$\text{LT}[\eta](\lambda) = \int_0^\infty ds\, \eta(s) e^{-\lambda s}. \tag{6}$$

The solution of this eigenvalue problem can be used to determine the discrete spectrum and hence whether the solution is stable (i.e. all eigenvalues reside in the left hand complex plane). In what follows we make explicit progress in solving the integral equations (4) and (5) by working with $w(\mathbf{r}) = w(r)$, where $r = |\mathbf{r}|$. To begin with we focus on rotationally symmetric solutions, and show how these may be obtained in closed form for the special case that the firing rate function is a Heaviside function, i.e. with $f(u) = H(u - h)$. Here the parameter h is identified as a firing threshold and $H(x) = 1$ for $x \geq 0$ and is zero otherwise. Moreover, we shall show that these solutions can undergo bifurcations to non-rotationally symmetric states (typically multi-bumps) with variation of the threshold parameter h. We note that it may also be possible to explicitly construct non-rotationally symmetric solutions with an osculating boundary between firing and non-firing regions if we consider piecewise constant rotationally symmetric synaptic (*top-hat*) kernels [16]. However, we shall not pursue this further here, though later in section 5 we will consider the numerical construction (and continuation) of non-rotationally symmetric multi-bump solutions.

3. Rotationally symmetric solutions

Rotationally symmetric solutions have the property that $q(\mathbf{r}) = q(r)$, and are a consequence of choosing a rotationally symmetric kernel. The stability of such solutions can be found by constructing the associated Evans function. Evans functions were first developed to study the stability of travelling waves in PDEs [11]. In essence the Evans function is an analytic tool whose zeros correspond to eigenvalues of the linearised problem obtained after considering perturbations around a localised solution. Moreover, the order of the zero and the multiplicity of the eigenvalue match. For examples of the use of Evans functions in systems with nonlocal interactions see [8, 28, 29].

3.1. Bump solutions

The first rotationally symmetric solution that we consider is a so-called one-bump solution described by the simple condition $q(r) > h$ for $r < a$ and $q(r) < h$ for $r > a$. Hence, from (4)

$$q(r) = \int_0^{2\pi} \int_0^a w(|\mathbf{r} - \mathbf{r}'|) r' \mathrm{d}r' \mathrm{d}\theta. \tag{7}$$

This is readily evaluated using a 2D Fourier transform (equivalent to a Hankel transform) of $w(\mathbf{r})$, which we write in the form

$$w(r) = \int_0^\infty \widetilde{w}(k) J_0(rk) k \mathrm{d}k. \tag{8}$$

Here $J_\nu(x)$ is the Bessel function of the first kind, of order ν and

$$\widetilde{w}(k) = \int_{\mathbb{R}^2} \mathrm{e}^{i\mathbf{k}\cdot\mathbf{r}} w(\mathbf{r}) \mathrm{d}\mathbf{r}. \tag{9}$$

Following [3, 12] it may then be shown that substitution of (8) into (7) gives

$$q(r) = 2\pi a \int_0^\infty \widetilde{w}(k) J_0(rk) J_1(ak) \mathrm{d}k. \tag{10}$$

Using the fact that $f'(u) = \delta(r - a)/|q'(a)|$ means that (5) reduces to

$$u(r, \theta) = \frac{a\mathrm{LT}[\eta](\lambda)}{|q'(a)|} \int_0^{2\pi} w(|\mathbf{r} - \mathbf{a}'|) u(a, \theta') \mathrm{d}\theta', \tag{11}$$

where $\mathbf{a}' = (a, \theta')$. We look for solutions of the form $u(r, \theta) = u_m(r) \mathrm{e}^{im\theta}$, where $m \in \mathbb{Z}$. In this case the radial component of the eigenfunction satisfies

$$\frac{u_m(r)}{u_m(a)} = \frac{a\mathrm{LT}[\eta](\lambda)}{|q'(a)|} \int_0^{2\pi} \cos(m\theta) w(\sqrt{r^2 + a^2 - 2ra\cos\theta}) \mathrm{d}\theta, \tag{12}$$

where we have exploited the fact that $\int_0^{2\pi} w(|\mathbf{r} - \mathbf{a}'|) \sin(m\theta) \mathrm{d}\theta = 0$. Hence, radial perturbations away from the border of the bump are completely determined by the perturbation at the bump edge (where $r = a$). Setting $r = a$ in (12) generates an implicit expression for the discrete spectrum $\lambda = \lambda_m$, where λ_m is the solution to

$$\mathcal{E}_m(\lambda) \equiv \mathrm{LT}[\eta](\lambda)^{-1} - \mu_m = 0, \tag{13}$$

with $\mu_m \in \mathbb{R}$ given by

$$\mu_m = \frac{2a}{|q'(a)|} \int_0^\pi w(2a\sin\theta) \cos(2m\theta) \mathrm{d}\theta. \tag{14}$$

We interpret $\mathcal{E}_m(\lambda)$ as a family of Evans functions for the two dimensional one-bump. The zeros of the Evans function determine the location of the point spectrum and can be used to determine solution stability (the essential spectrum being confined to the left-hand complex plane). It can be shown that i) the Evans function is only real-valued if the eigenvalue parameter λ is real, ii) the complex number λ is an eigenvalue of (5) if and only if $\mathcal{E}(\lambda) = 0$, and iii) the algebraic multiplicity of an eigenvalue is exactly equal to the order of the zero of the Evans function [8]. Also, from rotation invariance, $\mathcal{E}_1(0) = 0$. The condition for stability is thus that Re $(\lambda_m) < 0$ for all m. Although

it is hard to find closed form expressions for λ_m it is a simple matter to obtain them numerically.

An evaluation of the bump solution (7) in closed form is typically only possible for special choices of $w(r)$. In fact it is easier to choose forms of $\widetilde{w}(k)$ (the 2D Fourier transform of $w(\mathbf{r})$) that allow the use of known integral formulas involving products of Bessel functions. From the analysis of one dimensional stationary solutions [2] we would expect to obtain bump solutions for a rotationally symmetric kernel of the form $w(r) = e^{-r} - e^{-r/2}/4$. Since this two dimensional Mexican hat function does not have a simple Hankel transform we make use of the approximation

$$\frac{1}{2\pi}e^{-r} \approx \frac{2}{3\pi}\left(K_0(r) - K_0(2r)\right) \equiv E(r), \tag{15}$$

where $K_\nu(x)$ is the modified Bessel function of the second kind of order ν. For computational simplicity we now work with the explicit choice $w(r) = E(r) - E(\beta r)/\gamma$. Here $\beta < 1$ and $\gamma > 1$ gives the typical Mexican hat profile. In this case $\int_{\mathbb{R}^2} w(|\mathbf{r}|)d\mathbf{r} = (\gamma\beta^2 - 1)/(2\pi\gamma\beta^2)$. Hence, the kernel is *balanced* when $\gamma = 1/\beta^2$ so that $\int_{\mathbb{R}^2} w(|\mathbf{r}|)d\mathbf{r} = 0$. Using the fact that the Hankel transform of $K_0(pr)$ is $H_p(k) = (k^2 + p^2)^{-1}$ we may write

$$\widetilde{w}(k) = \frac{2}{3\pi}\left\{H_1(k) - H_2(k) + \frac{H_{2\beta}(k)}{\gamma} - \frac{H_\beta(k)}{\gamma}\right\}. \tag{16}$$

Substitution into (10) leads to integrals of the form

$$\int_0^\infty \frac{J_0(rk)J_1(ak)}{k^2 + p^2}dk \equiv L_p(a, r). \tag{17}$$

Integrals of this type are given by [12, 33]

$$L_p(a, r) = \begin{cases} \frac{1}{p}I_1(pa)K_0(pr) & r \geq a \\ \frac{1}{ap^2} - \frac{1}{p}I_0(pr)K_1(pa) & r < a \end{cases}, \tag{18}$$

where $I_\nu(x)$ is the modified Bessel function of the first kind, of order ν. Using the above allows us to compute (10) as $q(r) = q(r; a)$, with

$$q(r; a) = \frac{4a}{3}\left(L_1(a, r) - L_2(a, r) + \frac{L_{2\beta}(a, r)}{\gamma} - \frac{L_\beta(a, r)}{\gamma}\right). \tag{19}$$

The bump radius is determined by the condition $q(a) = h$. In Figure 1 we plot the bump radius as a function of firing threshold for $\beta = 0.5$ and three choices of γ so that $\int_{\mathbb{R}^2} w(|\mathbf{r}|)d\mathbf{r}$ is negative ($\gamma\beta^2 - 1 < 0$), zero ($\gamma\beta^2 - 1 = 0$), and positive ($\gamma\beta^2 - 1 > 0$). In each case there are two branches of solution. Moreover, on the upper branch we can distinguish two qualitatively different shapes of solution; one with $q''(0) < 0$ for $h > h_D$ and the other with $q''(0) > 0$ for $h < h_D$. We shall refer to the latter as a *dimpled* solution. Typical shapes for dimpled and non-dimpled solutions are shown in the insets of Figure 1. Also, on the upper branch of Figure 1 we have plotted the point at which $q''(0) = 0$, defining the transition from dimpled to non-dimpled solutions at $h = h_D$.

We now consider the possibility of instabilities on these branches of bump solutions, with an exponential synaptic time course $\eta(t) = \alpha e^{-\alpha t}H(t)$. In this case $\text{LT}[\eta](\lambda)^{-1} = 1 + \lambda/\alpha$. Without loss of generality, in this section we now set $\alpha = 1$. The condition

for stability is simply that $\lambda_m < 0$ for all m, where $\lambda_m = -1 + \mu_m$. In Figure 2 we plot λ_0, λ_2 and λ_3 along the $\gamma = 4$ solution branch of Figure 1 (λ_1 is identically zero by rotation invariance). This shows that the lower branch $a = a_-$ is unstable even to rotationally symmetric perturbations ($m = 0$), and that the upper branch a_+ is stable to such perturbations (since $\lambda_0 < 0$ on a_+). In addition, on a_+ there is a loss of stability as h decreases, firstly at $h = h_D = 0.094$ to perturbations with $m = 2$, and then to perturbations with $m = 3$. In the $\gamma = 4$ case, λ_2 crosses through zero precisely at the point $h = h_D$ on a_+, signalling the fact that dimple solutions are unstable. However, changes in stability do not coincide with the transition to dimple bumps when $\int_{\mathbb{R}^2} w(|\mathbf{r}|)\mathrm{d}\mathbf{r} \neq 0$ (e.g. for $\gamma = 3$ and $\gamma = 5$, as illustrated in Figure 1).
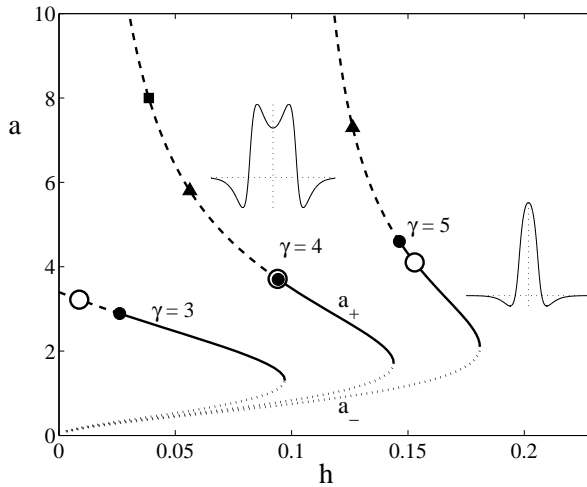

Figure 1. Bump radius a as a function of threshold h, for weight kernels $w(r) = E(r) - E(\beta r)/\gamma$ with $\beta = 0.5$ and $\gamma = 3, 4, 5$ (for which $\int_{\mathbb{R}^2} w(|\mathbf{r}|)\mathrm{d}\mathbf{r}$ is positive, zero, and negative respectively). In each case narrow and wide bumps may coexist, but the narrow (lower) branch is always unstable (dotted lines). As h decreases along the wide (upper) branches the stable bump (solid lines) loses stability with dominant mode $m = 2$ (solid circles), then $m = 3$ (triangles), then $m = 4$ (squares), etc. Note that for $h < h_D$ the bump solution on the branch a_+ has a *dimple*. The point where $h = h_D$ on the upper branch is indicated by the open circle, and coincides with the change of stability when $\gamma = 4$.

From the shape of the eigenfunction $u_2(r)\cos 2\theta$, plotted in Figure 3, we would expect the bump to go unstable in favor of a double bump solution as h is decreased through h_D. Indeed direct numerical simulations confirm this prediction, and Figure 3 shows the emergent state at h just less than h_D, when a one-bump solution is perturbed with a linear combination of the modes $u_2(r)\cos 2\theta$ and $u_3(r)\cos 3\theta$ (showing that $m = 2$ modes are amplified and $m = 3$ modes are suppressed at bifurcation). Calculations of the Evans function for $\gamma = 3$ also indicate such instabilities, but as indicated in Figure 1, mode 2 instabilities develop even for non-dimpled bumps. In this case direct numerical simulations show an initial single bump splitting in two, and then splitting twice more to yield eight bumps (see Figure 4).
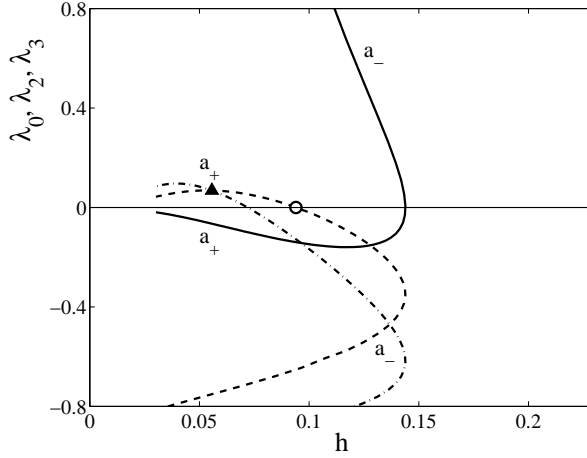
Figure 2. A plot of λ_0 (solid line), λ_2 (dashed line) and λ_3 (dot-dashed line) along the existence curve for bumps with $\gamma = 4$ (see Figure 1). We note that $\lambda_1 = 0$ for all points on the curve $a = a(h)$. Hence, although solutions on a_+ are stable to rotationally symmetric perturbations ($\lambda_0 < 0$), at $h = h_D$ solutions lose stability to perturbations of the form $u_2(r)\cos(2\theta)$, and for smaller h mode 3 perturbations become dominant (solid triangle, corresponding to the similarly marked point on the $\gamma = 4$ branch of Figure 1).

Simulation for the balanced kernel (with $\beta = 0.5$ and $\gamma = 4$) when the dominant mode is predicted to be $m = 3$, leads, as expected, to theemergence of a pattern with three-fold rotational symmetry (Figure 5). In addition, the solution continues to develop a complex labyrinthine pattern throughout the domain.

3.2. Ring solutions

In a similar fashion as for one-bump solutions we may construct ring solutions which satisfy $q(r) \geq h$ only for $r \in D \subseteq (0, \infty)$. Assuming $q(\infty) < h$ we can write a one-ring solution in the form

$$q(r) = q(r; r_2) - q(r; r_1), \tag{20}$$

with $r_2 > r_1 > 0$. The description of the ring is completed with the simultaneous solution of the equations $q(r_1) = h = q(r_2)$.

To calculate the Evans function for ring solutions we proceed in exactly the same fashion as in section 3.1. It is straight forward to show that the radial component of the eigenfunction satisfies

$$\frac{u_m(r)}{\text{LT}[\eta](\lambda)} = \sum_{j=1}^{2} A_j(r, m, \lambda) u_j, \tag{21}$$

where

$$A_i(r, m, \lambda) = \frac{r_i}{|q'(r_i)|} \int_0^{2\pi} \cos(m\phi) w(\sqrt{r^2 + r_i^2 - 2rr_i \cos\phi})\,\mathrm{d}\phi. \tag{22}$$
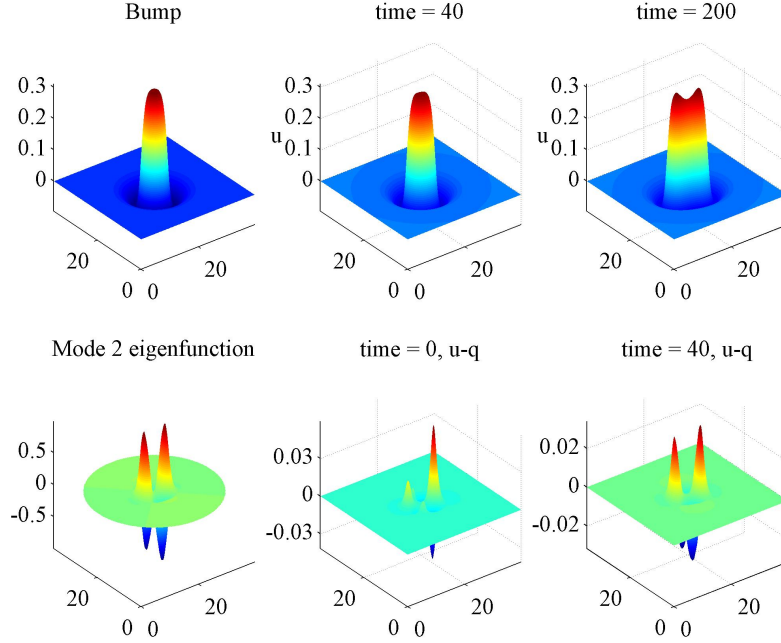
Figure 3. Top: A plot of the one-bump solution and its evolution following a perturbation with a linear combination of $m = 2$ and $m = 3$ modes, with $h = 0.09 < h_D = 0.094$. Bottom: The shape of the eigenfunction $u_2(r) \cos(2\theta)$ on the branch a_+ when $h = h_D = 0.094$, and the corresponding deviation of the solution (for $h = 0.09$) from the unstable stationary bump $(u(\mathbf{r}, t) - q(\mathbf{r}))$, which should reflect the shape of the eigenfunction. For $h < h_D$ a one-bump solution is predicted to be unstable with mode $m = 2$, and the simulations agree with this prediction. The other parameters are $a = 3.867$, $\beta = 0.5$, $\gamma = 4$.

Hence, radial perturbations are completely determined by the perturbation at the points (r_1, r_2). Demanding that the perturbations at r_j be non-trivial generates a family of Evans functions

$$\mathcal{E}_m(\lambda) = \left| \mathrm{LT}[\eta](\lambda)^{-1} I_2 - \mathcal{A}_m(\lambda) \right|, \tag{23}$$

where I_2 is the 2×2 identity matrix and $\mathcal{A}_m(\lambda)$ is a 2×2 matrix with components $[\mathcal{A}_m(\lambda)]_{ij} = A_j(r_i, m, \lambda)$, $i, j = 1, 2$.

As for the one-bump we find that there are regions of parameter space where two ring solutions can co-exist. Figure 6 shows the existence of ring solutions as h varies for $\beta = 0.5$ and four values of γ in the weight kernel $w(r) = E(r) - E(\beta r)/\gamma$. Examples of co-existing ring solutions are plotted (in profile) in the figure. A direct examination of the eigenspectrum (by tracing the zeros of the Evans function) shows that the lower branch of rings is always unstable to mode 0 perturbations. The upper branch is always stable to such rotationally symmetric perturbations, but for $\gamma < 4$ a sequence of instabilities has the fastest growing mode number increasing as h decreases. In Figure 7 we show an example where we plot the zero contours of Re $\mathcal{E}_m(\lambda)$ and Im $\mathcal{E}_m(\lambda)$, in the (ν, ω) plane, where we decompose $\lambda = \nu + i\omega$. The points at which the two curves cross define
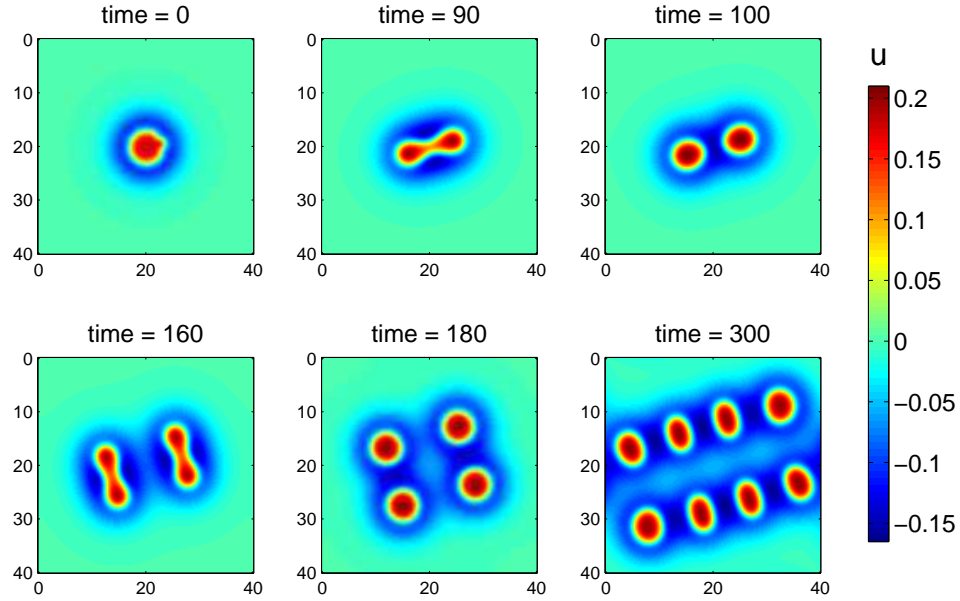
Figure 4. Repeated splitting of a bump solution. For these parameters ($h = 0.0149$, $a = 3.1$, $\beta = 0.5$, $\gamma = 3$) analysis of the Evans function predicts an instability with fastest growing mode $m = 2$.
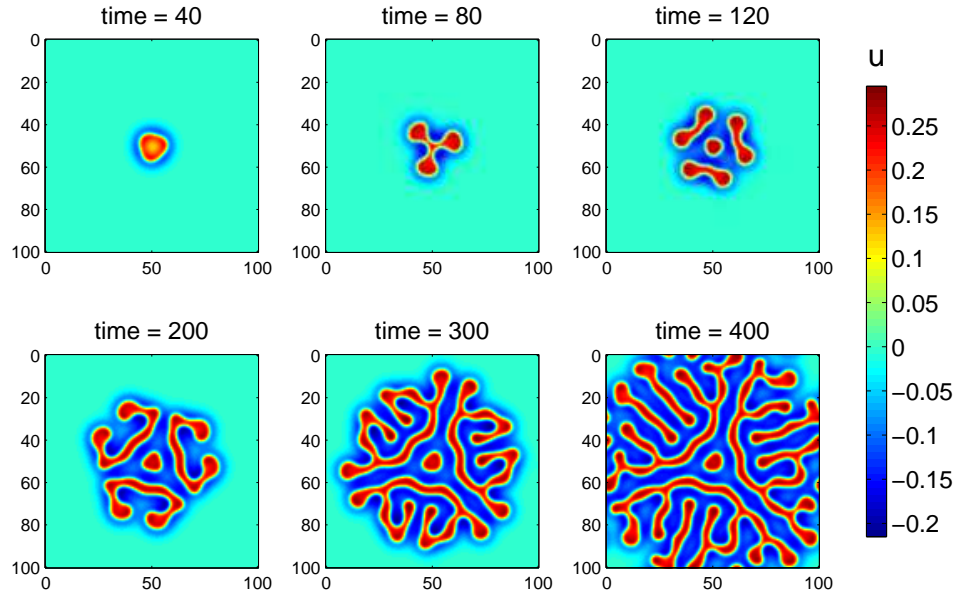

Figure 5. A mode three instability of a bump solution leads to a labyrinthine pattern throughout the domain. The parameters were $h = 0.05$, $\beta = 0.5$, and $\gamma = 4$ (corresponding to a bump radius of $a = 6.4$). Analysis of the Evans function predicts an instability with fastest growing mode $m = 3$.
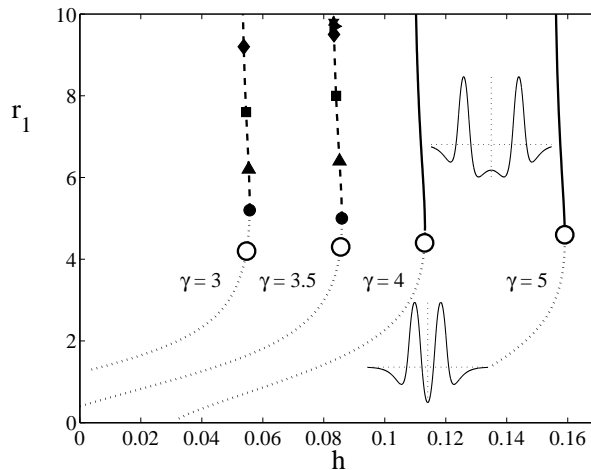
Figure 6. Existence and stability of ring solutions as h varies. Each curve shows the inner ring radius r_1 for the indicated value of γ, where the weight kernel is $w(r) = E(r) - E(\beta r)/\gamma$ with $\beta = 0.5$. In each case small and large rings may coexist, but calculations of the Evans function show that the small (lower) branch is always unstable (dotted lines). As h decreases along the larger (upper) branches the stable ring (solid lines) loses stability with dominant mode=2 (solid circles), then 3 (triangles), then 4 (squares), etc. Note that the ring solution develops a "dimple" (i.e. $q''(0) < 0$) at the points indicated by an open circle, but this does not necessarily coincide with the change of stability.

a zero of $\mathcal{E}_m(\lambda)$ and hence an eigenvalue. This plot shows that (for the given threshold) there is an instability with a fastest growing mode of $m = 5$.

In Figure 8 we show a two dimensional plot of an unstable ring solution, and the emergent structure of five bumps seen beyond instability. To explore the dependence of mode selection on the choice of threshold we plot in Figure 9 the values of the dominant eigenvalues of modes $m = 0, \ldots, 8$, with different choices of threshold value. It can be seen that as h decreases the dominant mode increases from 4 to 7. Figure 10 shows the mode 7 pattern that emerges from the ring with $h = 0.0534$, as predicted by our stability analysis. We note that results similar to those presented in Figures 8-10 were previously presented in [20], though in this work stability was found by numerical integration of the linearised equation, and did not utilise an Evans function approach.

It is also interesting to note that instabilities of axisymmetric ring solutions and their destabilisation into spots has also been observed in the two dimensional Gray-Scott model. Here a method to determine the number of resulting spots (multi-bumps) has also been developed, though this requires the solution of a nonlocal eigenvalue problem [24].

4. Lyapunov function

As observed in previous work of Laing and Troy [20], instabilities of localised structures can ultimately lead to the generation of multi-bump solutions where a finite number of
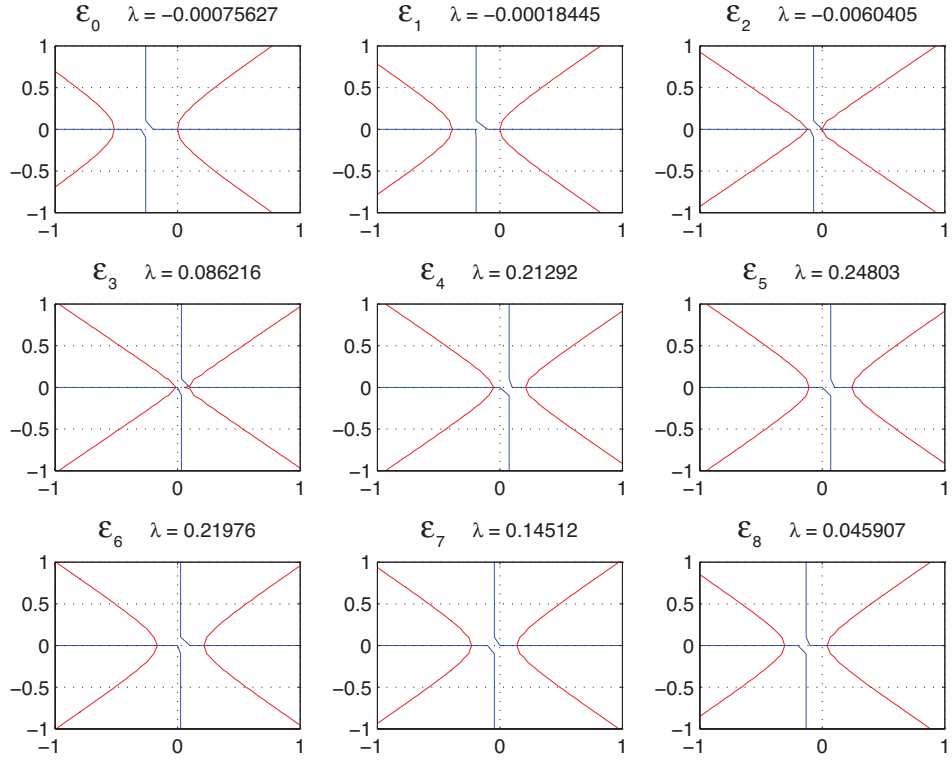
Figure 7. The zero contours of $\mathcal{E}_m(\lambda)$ $(m = 0, \ldots, 8)$ in the complex plane for the ring solution with $h = 0.0549$ and $\gamma = 3$ shown in Figure 6. Eigenvalues are found where contours cross. The value of λ above each subplot shows the value of the dominant eigenvalue for the mth mode. Clearly mode $m = 5$ is dominant.
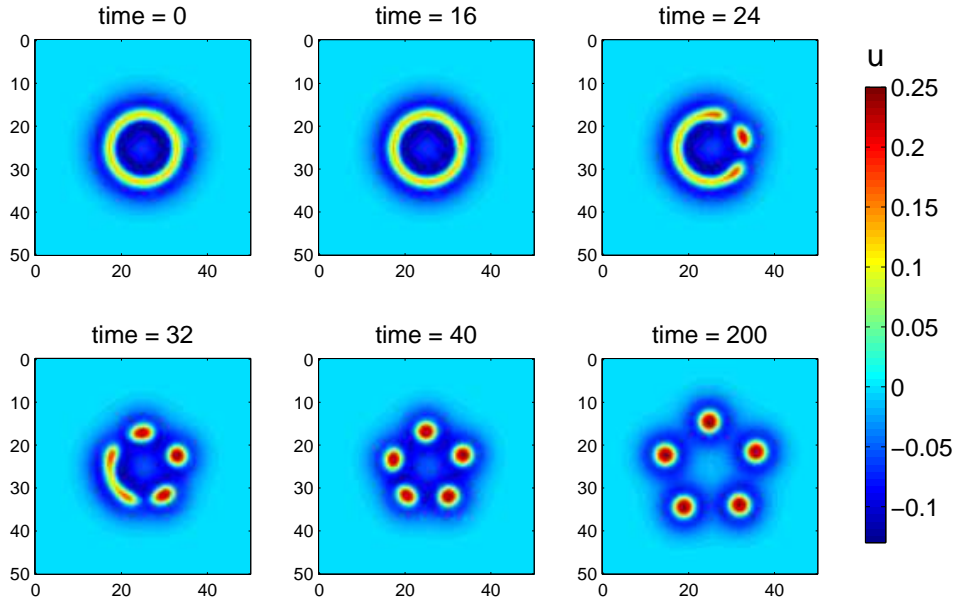

Figure 8. A plot of the emergent structure seen in direct numerical solutions after perturbing a ring solution with a linear combination of modes $0, 1, 2, \ldots 8$. The parameters correspond to Figure 7, and mode 5 is dominant, as expected: $h = 0.0549$, $r_1 = 7.0$, $r_2 = 8.63$, $\beta = 0.5$, $\gamma = 3$.
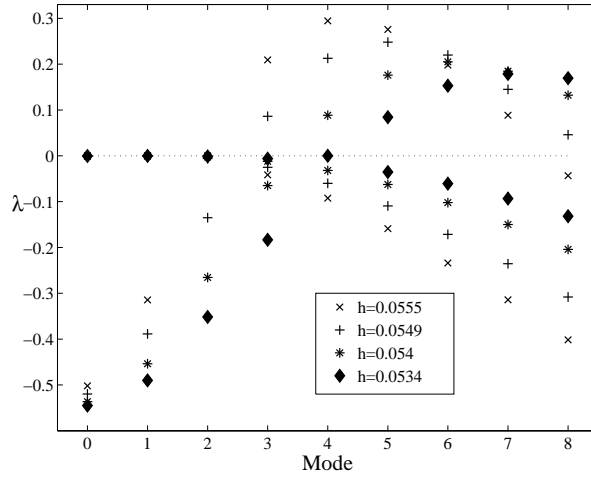
Figure 9. A plot of the first two dominant eigenvalues for ring solutions for different choices of h, illustrating how the dominant mode changes as h varies. As h decreases the dominant mode increases from 4 to 7. Here $\beta = 0.5, \gamma = 3$ in the weight kernel $w(r) = E(r) - E(\beta r)/\gamma$.
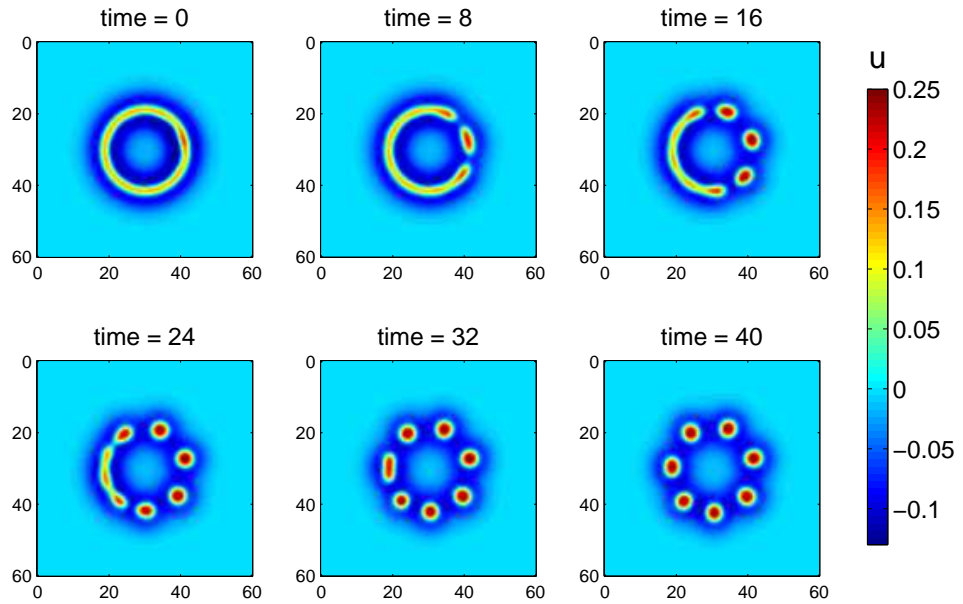

Figure 10. A series of plots showing the instability of a ring solution. Initial conditions are the ring plus a linear combination of modes $m = 0, \ldots, 8$. Mode 7 is predicted to be dominant, and the ring does evolve to a concentric set of 7 spots. $h = 0.0534$, $r_1 = 10.4$, $r_2 = 12.1$, $\beta = 0.5$, $\gamma = 3$.

bumps self-organise, sometimes into regular symmetric structures (such as in Figures 8 and 10). We now show that this self-organisation is directly linked to the minimisation of a Lyapunov function. For simplicity let us again consider an exponential synapse $\eta(t) = \alpha e^{-\alpha t} H(t)$ so that we may re-write (1) in the integro-differential form

$$\frac{1}{\alpha}\frac{\partial u(\mathbf{r},t)}{\partial t} = -u(\mathbf{r},t) + \int d\mathbf{r}' w(|\mathbf{r}-\mathbf{r}'|)f(u(\mathbf{r}',t)). \tag{24}$$

The natural generalisation of the Hopfield Lyapunov function [17] for discrete networks to continuous networks can be written [13]

$$E[u] = -\frac{1}{2}\int d\mathbf{r}\int d\mathbf{r}' w(|\mathbf{r}-\mathbf{r}'|)f(u(\mathbf{r},t))f(u(\mathbf{r}',t)) \tag{25}$$

$$+ \int d\mathbf{r}\int_0^{u(\mathbf{r},t)} ds\, f'(s)s. \tag{26}$$

For the choice of a Heaviside firing rate function $f(u) = H(u-h)$ this reduces to

$$E[u] = -\frac{1}{2}\int d\mathbf{r}\int d\mathbf{r}' w(|\mathbf{r}-\mathbf{r}'|)H(u(\mathbf{r},t)-h)H(u(\mathbf{r}',t)-h)$$

$$+ h\int d\mathbf{r}\, H(u(\mathbf{r},t)-h). \tag{27}$$

In Figure 11 we track the above Lyapunov function during the repeated splitting of a bump, previously illustrated in Figure 4. Each splitting event is accompanied by a rapid decrease in the Lyapunov function, which decreases as expected throughout this evolution. Figure 12 illustrates the decrease in the Lyapunov function associated
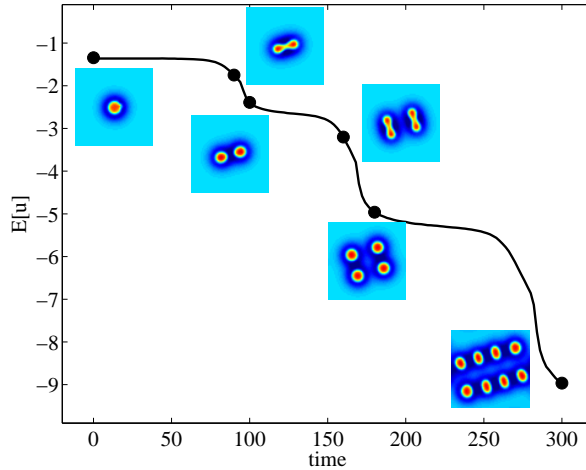

Figure 11. A plot of the Lyapunov function, $E[u]$, given by equation (27), during the repeated bump splitting illustrated in Figure 4—snapshots of that simulation are reproduced here for ease of reference. Each splitting is accompanied by a significant decrease in $E[u]$.

with an instability of a ring solution that gives rise to a pattern of 7 spots. We have also checked that this Lyapunov function decreases in a similar manner for all our simulations, including the development of labyrinthine patterns (previously illustrated in Figure 5).
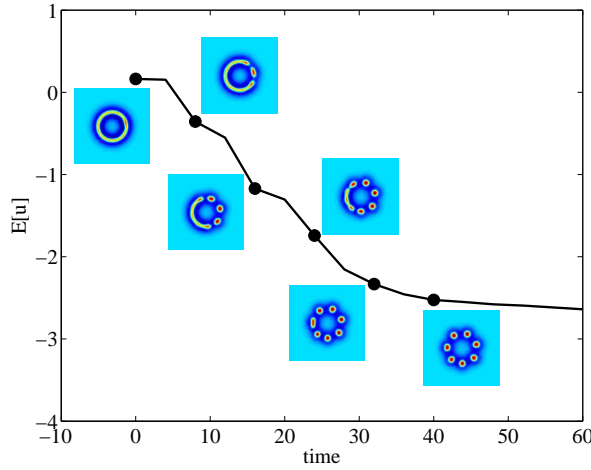
Figure 12. A plot of the Lyapunov function, $E[u]$, given by equation (27), during the splitting of an unstable ring into 7 spots, illustrated in Figure 10—the snapshots are reproduced here for ease of reference.

Figure 12, amongst others, shows how a rotationally symmetric state may destabilise in favour of a non-rotationally symmetric solution. The natural question arises as to whether such structures can undergo further instabilities. In the next section we show that the addition of a linear feedback term can destabilise such solutions in favour of rotating waves.

5. A model with spike frequency adaptation

In real neuronal tissue there are an abundance of metabolic processes whose combined effect may be modelled in terms of local feedback mechanisms that modulate synaptic currents. Here we consider a vector model with simple linear feedback dynamics, often invoked as a description of so-called *spike frequency adaptation* (SFA) [22]. An additional phenomenological current is included on the right hand side of the scalar model (24), so that

$$\frac{1}{\alpha}\partial_t u(\mathbf{r},t) = -u(\mathbf{r},t) + \int_{\mathbb{R}^2} \mathrm{d}\mathbf{r}w(|\mathbf{r}-\mathbf{r}'|)f(u(\mathbf{r}',t)) - ga(\mathbf{r},t), \qquad (28)$$

$$\partial_t a(\mathbf{r},t) = -a(\mathbf{r},t) + u(\mathbf{r},t). \qquad (29)$$

This model is a special case of the original Wilson-Cowan model [35, 36], and has been extensively studied in one dimension with regards to travelling wave solutions [27, 7, 8], and in two-dimensions with regards to rotationally symmetric localised solutions [12] and spiral waves [19]. Here, however, we study the effect of such linear adaptation on the stability of non-rotationally symmetric states. This is motivated by unpublished numerical observations of Troy and Laing which have shown bifurcations to rotating waves. Using a general argument, based on work of Moskalenko *et. al.* [25] for the rotational bifurcation of localised states in a three-component reaction-diffusion system (with one activator and two inhibitors), we show, regardless of connectivity pattern or

choice of firing rate function, that as long as a non-rotationally symmetric solution exists then it will destabilise to a rotating wave as g is increased through $g_c = 1/\alpha$.

5.1. Rotational Bifurcation

We begin by writing time-independent solutions of (28)-(29) as $u(\mathbf{r}, t) = q(\mathbf{r})$, where

$$q(\mathbf{r}) = \frac{1}{1 + g} \int_{\mathbb{R}^2} \mathrm{d}\mathbf{r} w(|\mathbf{r} - \mathbf{r}'|) f(q(\mathbf{r}')). \tag{30}$$

Note that there is a one-to-one correspondence between steady states of the scalar model (1) and the vector model (28)-(29) (up to a rescaling by $1 + g$).

Linearising about (30) gives

$$\partial_t \psi(\mathbf{r}, t) = \mathcal{L}[\overline{\psi}] \psi, \quad \psi = \begin{pmatrix} u(\mathbf{r}, t) \\ a(\mathbf{r}, t) \end{pmatrix}, \quad \overline{\psi} = \begin{pmatrix} q(\mathbf{r}) \\ q(\mathbf{r}) \end{pmatrix}, \tag{31}$$

where

$$\mathcal{L}[\overline{\psi}] = M + \alpha w \otimes f'(q) \begin{pmatrix} 1 & 0 \\ 0 & 0 \end{pmatrix}, \quad M = \begin{pmatrix} -\alpha & -\alpha g \\ 1 & -1 \end{pmatrix}. \tag{32}$$

From invariance of the full system (under rotation and translation) there exists a Goldstone mode $\psi_0 = \partial_\theta \overline{\psi}$ such that

$$\mathcal{L}\psi_0 = 0. \tag{33}$$

One of the possible destabilisations of $\overline{\psi}$ occurs when one of the other modes exactly coincides with ψ_0 under parameter variation. Because of this parameter degeneracy a generalised eigenfunction ψ_1 of $\mathcal{L}$ appears:

$$\mathcal{L}\psi_1 = \psi_0. \tag{34}$$

The solvability condition for this equation leads to an equation defining the bifurcation point in the form

$$\langle \psi_0^\dagger \mid \psi_0 \rangle = 0, \tag{35}$$

where $\langle \cdot \mid \cdot \rangle$ denotes inner product and $\psi_0^\dagger$ is the eigenfunction of the operator $\mathcal{L}^\dagger$ with zero eigenvalue. Here, $\mathcal{L}^\dagger$ is adjoint to, and has the same symmetry properties as, $\mathcal{L}$. In the Appendix we show that $\psi_0^\dagger$ can be written in closed form as a linear transformation of ψ_0. Because of this relationship the inner product in equation (35) can be easily calculated, giving

$$0 = (\alpha g - 1) \left\langle f'(q)(\partial_\theta q)^2 \right\rangle. \tag{36}$$

Hence, provided a non-rotationally symmetric solution of (28)-(29) exists, it will lose stability as g increases through $g_c = 1/\alpha$. Although we have not proven the existence of non-rotationally symmetric solutions, this can be inferred from the numerical simulations in Section 3.2 (see Figures 8 and 10). In fact the analysis above holds for both rotational and translational (drift) instabilities, and the dynamics beyond the bifurcation point is determined by both translational and rotational modes as well as their interaction.

5.2. Numerical example

We consider the model (28)-(29) with

$$w(r) = \int_0^\infty \frac{s J_0(rs)}{0.1 + (s^2 - 1)^2} \, \mathrm{d}s, \tag{37}$$

where $f(u) = 0.4 H(u - 0.25) \exp\left[-0.1/(u - 0.25)^2\right]$. The coupling function (37) is plotted in Figure 13a. The reason for using a coupling function of this form is that (37) has a Hankel transform with a rational structure, namely $\widetilde{w}(k) = 1/(0.1 + (k^2 - 1)^2)$. Taking the 2D spatial Fourier transform of equation (28) (which we denote with the symbol FT) and rearranging gives

$$[(k^2 - 1)^2 + 0.1]\mathrm{FT}[u + ga + \alpha^{-1}\partial_t u] = \mathrm{FT}[f(u)]. \tag{38}$$

After performing the inverse Fourier transform we have the equivalent PDE model

$$[\nabla^4 + 2\nabla^2 + 1.1](u + ga + \alpha^{-1}\partial_t u) = f(u). \tag{39}$$

Stationary solutions of (28)-(29) then satisfy

$$(1 + g)[\nabla^4 + 2\nabla^2 + 1.1]u = f(u), \qquad a = u. \tag{40}$$

To study uniformly rotating solutions of (28)-(29), one replaces $\partial/\partial t$ by $-\omega \times \partial/\partial\theta$, where ω is the angular velocity. Rotating solutions then satisfy

$$[\nabla^4 + 2\nabla^2 + 1.1]\left(1 - \frac{\omega}{\alpha}\frac{\partial}{\partial\theta} + g\left(1 - \omega\frac{\partial}{\partial\theta}\right)^{-1}\right)u = f(u), \tag{41}$$

$$a = \left(1 - \omega\frac{\partial}{\partial\theta}\right)^{-1}u. \tag{42}$$

The stability of a stationary solution, $(\widehat{u}, \widehat{a})$, is determined by the rightmost few eigenvalues of the Jacobian

$$J_1(\widehat{u}) = \begin{pmatrix} -\alpha + \alpha K^{-1}f'(\widehat{u}) & -g\alpha \\ 1 & -1 \end{pmatrix}, \tag{43}$$

where $K = \nabla^4 + 2\nabla^2 + 1.1$. Similarly, the stability of a rotating solution, $(\bar{u}, \bar{a})$, is determined by the rightmost few eigenvalues of the Jacobian

$$J_2(\bar{u}) = \begin{pmatrix} -\alpha + \omega\frac{\partial}{\partial\theta} + \alpha K^{-1}f'(\bar{u}) & -g\alpha \\ 1 & \omega\frac{\partial}{\partial\theta} - 1 \end{pmatrix}. \tag{44}$$

Solutions of (40) and (41) are found numerically by discretising the domain using polar coordinates and then integrating (28)-(29) to either a steady state or rotating solution. We then use pseudo-arclength continuation to follow solutions as parameters are varied. See [21, 20, 19] for more details on this approach.

In Figure 13b we show a plot of a stationary non-rotationally symmetric three-bump solution, calculated as described above for $g = 0$. As predicted, the solution in Figure 13b begins to rotate as g is increased through g_c. Since our instability analysis predicts that the rotational instability is degenerate with a translational mode simulations are done on a circular domain with Neumann boundary conditions, so as to
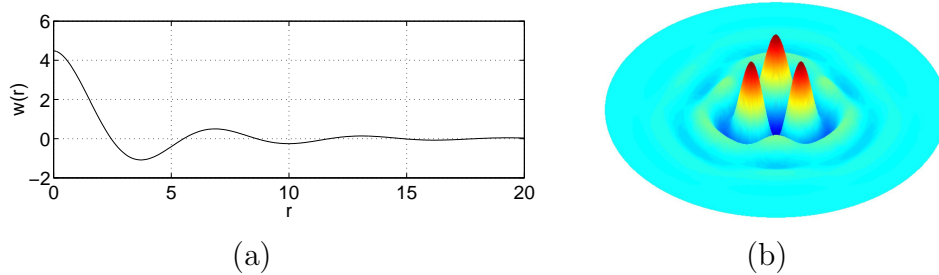
Figure 13. (a) The coupling function $w(r)$, given by (37). (b) A stationary three-bump solution of (28)-(29). The domain has radius 25.

favour seeing a rotation (as opposed to a drift). Our results from numerical continuation are shown in Figure 14. The top panel shows the maximum of u over the whole domain as a function of g for a stationary three-bump solution. We have chosen two different values of α ($\alpha = 5$ and $\alpha = 6$) and computed the branches of rotating waves that bifurcate from the stationary solution. These branches are also shown in the top panel of Figure 14. Note that the rotating waves undergo saddle-node bifurcations as g is increased; we do not follow the branches much beyond these bifurcations. We can see from this panel that (for the parameter values used) if α was smaller than about 4.5 we would not see a transition from stationary to rotating three-bump solution as g was increased, since the stationary solution would be destroyed in a saddle-node bifurcation before g reached g_c.

The middle panel shows the real part of the rightmost few eigenvalues of the Jacobian $J_1(\widehat{u})$ for both values of α chosen, as a fuction of g. A single real eigenvalue passes through zero as g increases through g_c ($= 1/\alpha$). We have also checked that this occurs for several other values of α (not shown). Note that there is always a zero eigenvalue as expected, due to the rotational invariance of the system. The eigenfunction corresponding to the eigenvalue that passes through zero (not shown) is proportional to $\partial \widehat{u}/\partial \theta$, as expected.

The bottom panel of Figure 14 shows ω as a function of g for the two branches of rotating solutions shown in the top panel. Evaluation of the eigenvalues of $J_2(\bar{u})$ along these branches shows that they are stable until the saddle-node bifurcations at high g (not shown). Finally, Figure 15 shows a series of snapshots showing the evolution of an unstable three-bump solution which rotates and translates on a large domain, before it ultimately reaches the boundary of the domain and induces the spread of a regular global pattern.

6. Discussion

In this paper we have shown the importance of considering angular perturbations in two-dimensional neural field models. In the simplest case of a bump solution and a Heaviside firing rate function, in one space dimension the upper branch of bump solutions is always stable, yet in two space dimensions we find, using the theory of Evans functions, that
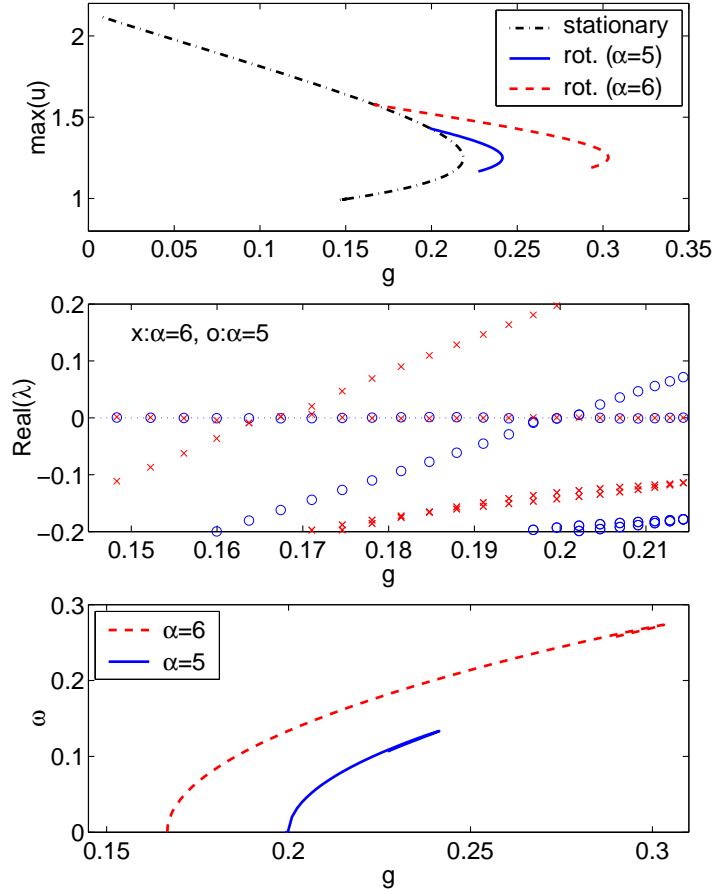
Figure 14. Rotational instability of a three-bump solution. Top: the branch of stationary solutions, and two representative branches of rotating solutions that bifurcate from it when $\alpha = 5$ and when $\alpha = 6$. Middle: real part of the rightmost few eigenvalues of the Jacobian for $\alpha = 5$ (circles) and $\alpha = 6$ (crosses). Bottom: angular velocity as a function of g for the rotating waves that appear when $\alpha = 5$ (solid) and when $\alpha = 6$ (dashed). Both branches are stable at their creation. Note the different horizontal scales for the three panels.

rotationally symmetric bump solutions can lose stability to perturbations of the form $u_m(r)\cos(m\theta)$, with the dominant mode depending on the model parameters. Typically we see an initial instability to mode two perturbations as the firing threshold h decreases below some critical value, followed by a sequence in which the dominant mode number increases as h decreases. In the case of a balanced weight kernel (i.e. $\int_{\mathbb{R}^2} w(|\mathbf{r}|)\mathrm{d}\mathbf{r} = 0$) we find that the onset of a bump instability occurs when the bump develops a central *dimple*. However, the appearance of a dimple does not necessarily coincide with onset of instability in the case of unbalanced kernels. In some cases the predicted bump instability leads to the bump splitting in two, and the two-bump solution that emerges splits once again, and so on. This feature is reminiscent of spot splitting in the Gray-Scott reaction-diffusion system [26]. We also see the emergence of labyrinthine patterns from a bump that is unstable to mode 3 perturbations (Figure 5), again a feature that has been observed in reaction-diffusion systems [15].
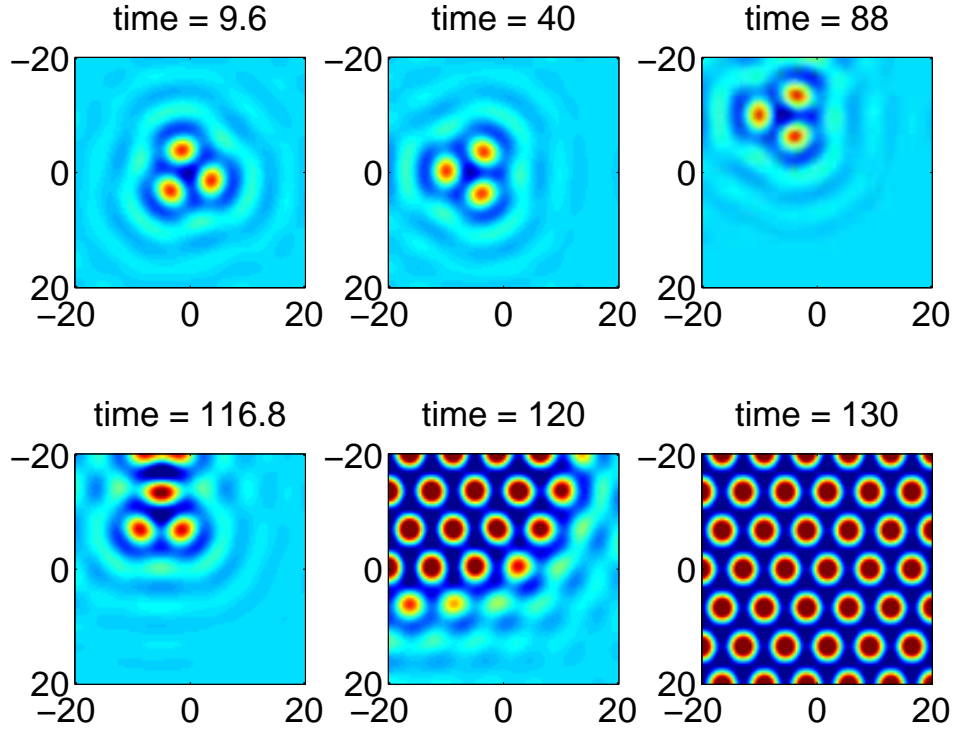
Figure 15. Instability of a stationary three-bump solution of (28)-(29) with coupling function $w(r)$ given by (37), and firing rate function $f(u) = 0.4H(u - 0.25)\exp\left[-0.1/(u - 0.25)^2\right]$. $\alpha = 5$ and g is switched from 0.19 to 0.22 at $t = 10$ and a small perturbation is applied. The three bump solution starts to rotate and translate, until it approaches the boundary and a regular pattern spreads across the whole domain.

Rotationally symmetric ring solutions $q(r)$ are defined in terms of two threshold crossings, where $q(r_1) = q(r_2) = h$. The evolution of a radial perturbation of mode m is determined by the perturbation at r_1 and r_2, and calculation of the associated Evans function shows that a lower branch of ring solutions is always unstable. On the upper branch instabilities develop with dominant unstable mode varying with h. Direct numerical simulations agree with the predictions of the stability analysis, with the dominant mode emerging from perturbations that combine many modes, and patterns developing with a corresponding number of bumps arranged in a circular fashion. Obviously it is also possible to construct other rotationally symmetric solutions, limited only by the requirement to simultaneously solve multiple threshold crossing conditions. It is also straightforward to generate a family of Evans functions that can be used to ascertain stability. Such solutions can include hybrid solutions such as a single bump with surrounding ring given by $q(r) = q(r; r_1) + q(r; r_4) - q(r; r_3)$, with $q(r) \geq h$ for $r \in [0, r_1] \cup [r_3, r_4]$, and a double-ring solution $q(r) = q(r; r_2) - q(r; r_1) + q(r; r_4) - q(r; r_3)$, with $r_4 > r_3 > r_2 > r_1 > 0$ such that $q(r_4) = q(r_3) = q(r_2) = q(r_1) = h$.

We have also shown that the evolution of solutions of the two dimensional neural field model (1), initiated by instabilities of rotationally symmetric bump and ring

solutions, correspond to the decrease of an associated Lyapunov function [13]. Given the emergence of non-rotationally symmetric solutions (e.g. 7 bumps on a circle, Figure 10), we found that such solutions could themselves become unstable to rotational and/or translational perturbations, using a Goldstone mode analysis. This technique is valid for arbitrary non-rotationally symmetric solutions, irrespective of their detailed shape. A potential tool to study the evolution of intricate structures such as the labyrinthine patterns seen here, is to formulate a description of the dynamics of the interface (where $u(\mathbf{r}, t) = h$), along the lines described for reaction diffusion equations in [15].

The techniques we have used are quite general and naturally apply to other homogeneous neural field models. In particular recently developed models with nonlinear adaptation [7] and nonlinear threshold accommodation [9] can be analysed. Further analysis of the properties of localised states in such neural field models is useful in that it may shed light on the mechanism of short term working memory [5, 21], and suggest practical implementations of sensorimotor loops for autonomous robot systems [23].

Appendix

Here we show how to calculate $\psi_0^\dagger$ in terms of ψ_0. Starting from the definitions in equation (32), we proceed by diagonalising $\mathcal{L}$ in terms of the right eigenvectors $v_\pm$ of the matrix M:

$$v_\pm = \begin{pmatrix} \alpha g \\ -(\alpha + \lambda_\pm) \end{pmatrix}, \tag{45}$$

where

$$\lambda_\pm = \frac{-(1 + \alpha) \pm \sqrt{(1 - \alpha)^2 - 4\alpha g}}{2}. \tag{46}$$

Performing the transformation

$$\widetilde{\psi}_0 = P^{-1}\psi_0 \qquad P = [v_+ \ \ v_-], \tag{47}$$

then gives the pair of equations

$$\lambda_\pm \phi_\pm + \chi_\pm w \otimes f'(q)[\phi_+ + \phi_-] = 0, \tag{48}$$

with $\widetilde{\psi}_0 = [\phi_+, \phi_-]$ and

$$\chi_\pm = \mp\alpha \frac{\alpha + \lambda_\mp}{\lambda_+ - \lambda_-}. \tag{49}$$

Turning now to the adjoint operator $\mathcal{L}^\dagger$, we use the fact that

$$\mathcal{L}^\dagger = M^\dagger + \alpha f'(q)w \otimes \begin{pmatrix} 1 & 0 \\ 0 & 0 \end{pmatrix}. \tag{50}$$

Again we proceed by diagonalising $\mathcal{L}^\dagger$, this time in terms of the right eigenvectors $w_\pm$ of $M^\dagger$:

$$w_\pm = \begin{pmatrix} 1 \\ (\alpha + \lambda_\pm) \end{pmatrix}. \tag{51}$$

In a similar fashion we find

$$\lambda_{\pm}\phi_{\pm}^{\dagger} + \chi_{\pm}f'(q)w \otimes [\phi_+^{\dagger} + \phi_-^{\dagger}] = 0, \tag{52}$$

with $[\phi_+^{\dagger}, \phi_-^{\dagger}] = R^{-1}\psi_0^{\dagger}$ and $R = [w_+ \quad w_-]$. An inspection of (48) and (52) yields the relationship $\phi_{\pm}^{\dagger} = f'(q)\phi_{\pm}$, giving

$$\psi_0^{\dagger} = f'(q)RP^{-1}\psi_0. \tag{53}$$

Substitution of (53) into (35) gives equation (36) in Section 5.1.

References

[1] S Amari. Homogeneous nets of neuron-like elements. *Biological Cybernetics*, 17:211–220, 1975.

[2] S Amari. Dynamics of pattern formation in lateral-inhibition type neural fields. *Biological Cybernetics*, 27:77–87, 1977.

[3] P C Bressloff. Spontaneous symmetry breaking in self-organizing neural fields. *Biological Cybernetics*, 93:256–274, 2005.

[4] P C Bressloff, J D Cowan, M Golubitsky, P J Thomas, and M Wiener. Geometric visual hallucinations, Euclidean symmetry and the functional architecture of striate cortex. *Philosophical Transactions of the Royal Society London B*, 40:299–330, 2001.

[5] C L Colby, J R Duhamel, and M E Goldberg. Oculocentric spatial representation in parietal cortex. *Cerebral Cortex*, 5:470–481, 1995.

[6] S Coombes. Waves, bumps and patterns in neural field theories. *Biological Cybernetics*, 93:91–108, 2005.

[7] S Coombes, G J Lord, and M R Owen. Waves and bumps in neuronal networks with axo-dendritic synaptic interactions. *Physica D*, 178:219–241, 2003.

[8] S Coombes and M R Owen. Evans functions for integral neural field equations with heaviside firing rate function. *SIAM Journal on Applied Dynamical Systems*, 34:574–600, 2004.

[9] S Coombes and M R Owen. Bumps, breathers, and waves in a neural network with spike frequency adaptation. *Physical Review Letters*, 94(148102), 2005.

[10] G B Ermentrout and J D Cowan. A mathematical theory of visual hallucination patterns. *Biological Cybernetics*, 34:137–150, 1979.

[11] J Evans. Nerve axon equations: IV The stable and unstable impulse. *Indiana University Mathematics Journal*, 24:1169–1190, 1975.

[12] S E Folias and P C Bressloff. Breathing pulses in an excitatory neural network. *SIAM Journal on Applied Dynamical Systems*, 3:378–407, 2004.

[13] D A French. Identification of a free energy functional in an integro-differential equation model for neuronal network activity. *Applied Mathematics Letters*, 17:1047–1051, 2004.

[14] P S Goldman-Rakic. Cellular basis of working memory. *Neuron*, 14:477–485, 1995.

[15] R E Goldstein, D J Muraki, and D M Petrich. Interface proliferation and the growth of labyrinths in a reaction-diffusion system. *Physical Review E*, 53(4), 1996.

[16] J M Herrmann, H Schrobsdorff, and T Geisel. Localized activations in a simple neural field model. *Neurocomputing*, 65:679–684, 2005.

[17] J J Hopfield. Neurons with graded response have collective computational properties like those of two-state neurons. *Proceedings of the National Academy of Sciences*, 81:3088–3092, 1984.

[18] K Kishimoto and S Amari. Existence and stability of local excitations in homogeneous neural fields. *Journal of Mathematical Biology*, 7:303–318, 1979.

[19] C R Laing. Spiral waves in nonlocal equations. *SIAM Journal on Applied Dynamical Systems*, 4:588–606, 2004.

[20] C R Laing and W C Troy. PDE methods for nonlocal models. *SIAM Journal on Applied Dynamical Systems*, 2:487–516, 2003.

[21] C R Laing, W C Troy, B Gutkin, and G B Ermentrout. Multiple bumps in a neuronal model of working memory. *SIAM Journal on Applied Mathematics*, 63:62–97, 2002.

[22] Y H Liu and X J Wang. Spike-frequency adaptation of a generalized leaky integrate-and-fire model neuron. *Journal of Computational Neuroscience*, pages 25–45, 2001.

[23] I Mikhailova and C Goerick. Conditions of activity bubble uniqueness in dynamic neural fields. *Biological Cybernetics*, 92:82–91, 2005.

[24] D S Morgan and T J Kaper. Axisymmetric ring solutions of the 2D Gray-Scott model and their destabilization into spots. *Physica D*, 192:33–62, 2004.

[25] A S Moskalenko, A W Liehr, and H G Purwins. Rotational bifurcation of localized dissipative structures. *Europhysics Letters*, 63:361–367, 2003.

[26] J E Pearson. Complex patterns in a simple system. *Science*, 261(5118):189–192, 1993.

[27] D J Pinto and G B Ermentrout. Spatially structured activity in synaptically coupled neuronal networks: I. Travelling fronts and pulses. *SIAM Journal on Applied Mathematics*, 62:206–225, 2001.

[28] D J Pinto, R K Jackson, and C E Wayne. Existence and stability of traveling pulses in a continuous neuronal network. *SIAM Journal on Applied Dynamical Systems*, 4:954–984, 2005.

[29] B Sandstede. Evans functions and nonlinear stability of travelling waves in neuronal network models. *International Journal of Bifurcation and Chaos*, to appear, 2007.

[30] P Tass. Cortical pattern formation during visual hallucinations. *Journal of Biological Physics*, 21:177–210, 1995.

[31] J G Taylor. Neural 'bubble' dynamics in two dimensions: Foundations. *Biological Cybernetics*, 80:393–409, 1999.

[32] J Tegner, A Compte, and X-J Wang. The dynamical stability of reverberatory neural circuits. *Biological Cybernetics*, 87:471–481, 2002.

[33] G N Watson. *A treatise on the theory of Bessel functions*. Cambridge University Press, 1952.

[34] H Werner and T Richter. Circular stationary solutions in two-dimensional neural fields. *Biological Cybernetics*, 85:211–217, 2001.

[35] H R Wilson and J D Cowan. Excitatory and inhibitory interactions in localized populations of model neurons. *Biophysical Journal*, 12:1–24, 1972.

[36] H R Wilson and J D Cowan. A mathematical theory of the functional dynamics of cortical and thalamic nervous tissue. *Kybernetik*, 13:55–80, 1973.